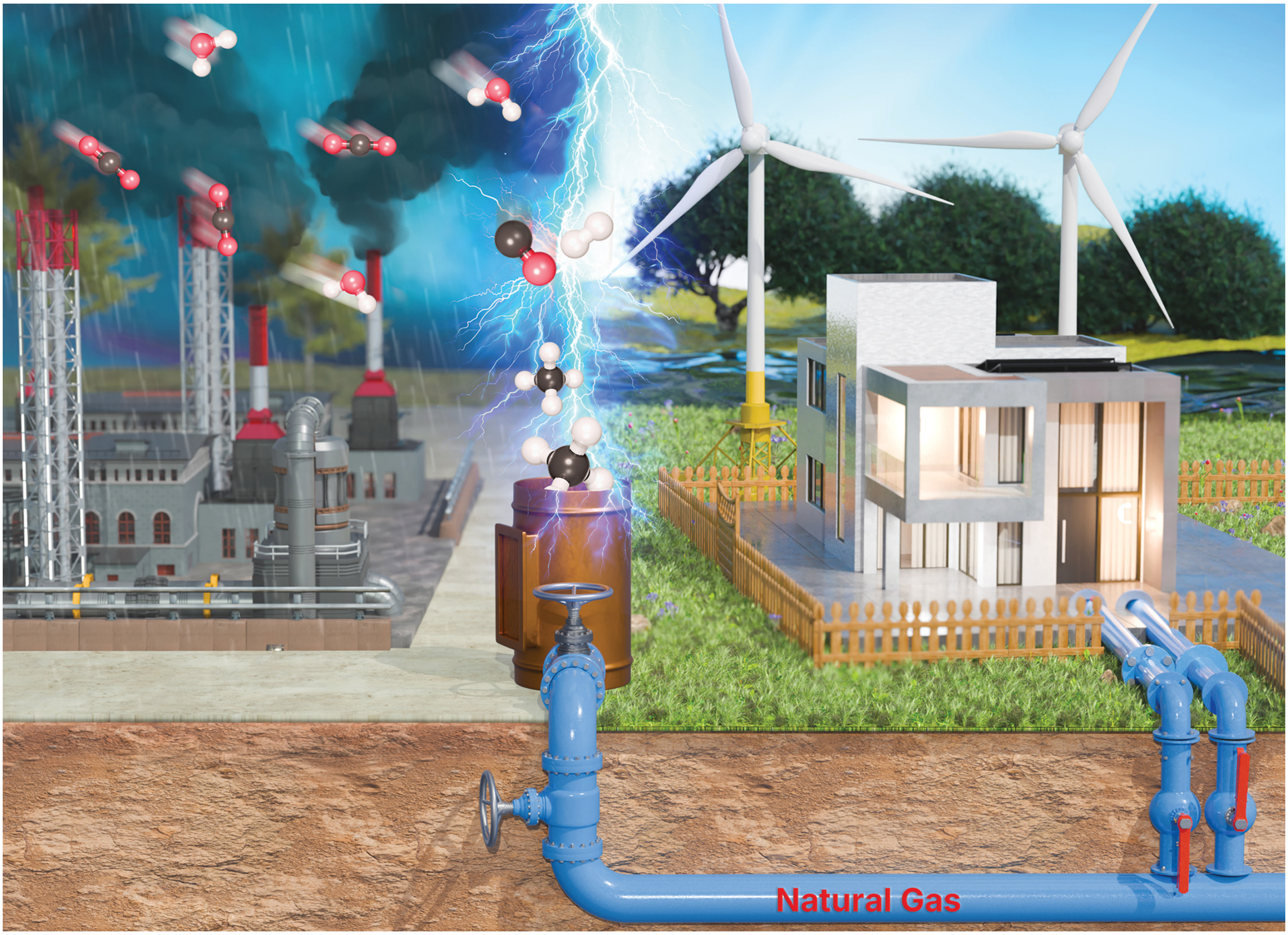

Showcasing research from Professor Dongil Lee's laboratory, Yonsei University, 50 Yonsei-ro, Seodaemun-gu, Seoul 03722, Republic of Korea.

High purity CH_4 production from CO_2 *via* cascade electro-thermocatalysis using metal nanoclusters with high CO_2 binding affinity

While methane is a desirable product due to its widespread use as a fuel, the direct electroreduction of CO_2 to CH_4 is hindered by challenges such as low product purity and high overpotentials. To overcome these limitations, we developed an efficient cascade system combining electrolysis and thermocatalysis for the high-purity production of CH_4 from CO_2. Electrochemical syngas generation using metal nanoclusters with high CO_2-binding affinity enabled near-theoretical single-pass conversion efficiency, followed by thermocatalytic conversion to high-purity methane.

Image reproduced by permission of Dongil Lee from *EES Catal.*, 2025, **3**, 723.

As featured in:

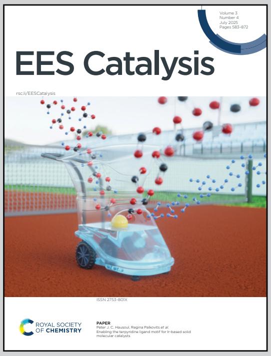

See Joonwoo Kim, Dongil Lee *et al.*, *EES Catal.*, 2025, **3**, 723.

ROYAL SOCIETY OF CHEMISTRY

rsc.li/EESCatalysis

EES Catalysis

ROYAL SOCIETY OF CHEMISTRY

PAPER

View Article Online
View Journal | View Issue

Check for updates

Cite this: *EES Catal.*, 2025, 3, 723

High purity CH_4 production from CO_2 *via* cascade electro-thermocatalysis using metal nanoclusters with high CO_2 binding affinity†

Sang Myeong Han,[a] Minyoung Park,[a] Seonju Kim,[a] Cheonwoo Jeong,[b] Joonwoo Kim*[b] and Dongil Lee *[a]

Received 29th March 2025,
Accepted 12th May 2025

DOI: 10.1039/d5ey00094g

rsc.li/eescatalysis

Electrochemical CO_2 reduction reaction (CO_2RR) has emerged as a promising strategy to convert CO_2 into value-added chemicals and fuels. While methane is especially desirable owing to its extensive use as a fuel, existing infrastructure, and large global market, the direct electroreduction of CO_2 to CH_4 is hindered by challenges such as low product purity and high overpotentials. In this study, an efficient cascade electrolysis and thermocatalysis system for the high-purity production of CH_4 from CO_2 has been demonstrated. Electrochemical syngas production was carried out using CO_2RR-active electrocatalysts, including Au_{25} and Ag_{14} nanoclusters (NCs). While both NCs exhibited high CO_2-to-CO activity in alkaline media, Ag_{14} NCs enabled syngas production with a varying ratio (H_2/CO) by adjusting the CO_2 flow rate, achieving near-theoretical single-pass conversion efficiency (SPCE) of over 45% (theoretical limit = 50%). Electrokinetic analysis revealed that the strong CO_2 binding affinity and exceptional CO selectivity of Ag_{14} NCs contribute to superior syngas tunability and carbon conversion efficiency. Electrochemically generated syngas ($H_2/CO = 3$) at 800 mA cm^{-2} was directly fed into a thermocatalysis reactor, producing CH_4 with a purity exceeding 85%.

Broader context

Converting CO_2 into deep-reduced chemicals and fuels is a promising strategy to address environmental issues and achieve a carbon-neutral society. Currently, electrochemical and thermocatalytic methods are extensively studied to develop efficient conversion processes, along with other approaches. However, electrochemical CO_2 conversion suffers from low product purity, while significant challenges remain in the energy-intensive CO production step *via* the reverse water–gas shift (RWGS) reaction in thermocatalytic conversion. We report an efficient cascade electro-thermocatalysis process that electrochemically converts CO_2 into syngas, followed by subsequent thermal CO methanation. This cascade system not only bypasses the energy-intensive RWGS reaction but also ensures high CH_4 purity in the product gas stream. Additionally, we present key design principles for electrocatalysts in electrochemical syngas production with near-theoretical single-pass conversion efficiency, enabled by the high CO_2 binding affinity of nanocluster electrocatalysts. This unique property allows tunable CO_2-free syngas production with various syngas ratios (H_2/CO) by adjusting the initial CO_2 flow rate. The electrochemically produced CO_2-free syngas is then converted into CH_4 with a purity exceeding 85% at an industrially relevant current density of 800 mA cm^{-2}. These findings establish the viability of the cascade electro-thermocatalysis system for high-purity chemical production with high carbon conversion efficiency.

Introduction

Electrochemical CO_2 reduction reaction (CO_2RR) has garnered significant interest as a promising strategy for converting CO_2 into valuable chemicals and fuels, while also serving to store surplus renewable energy.[1–3] Among several products derived from CO_2, CO production has garnered substantial research attention owing to its wide-ranging applications as a component of syngas (a mixture of CO and H_2) in numerous industrial processes, including methanation, alcohol production, and Fischer–Tropsch synthesis.[4–6] Furthermore, electrochemically produced CO (or syngas) can effectively mitigate sulfur and nitrogen contamination—issues commonly encountered in traditional fossil fuel-based methods such as natural gas reforming and coal gasification, which are also associated with significant pollution and high energy consumption.[7–10] Various Au- and Ag-based nanoparticles have been developed as selective

---

[a] *Department of Chemistry, Yonsei University, Seoul 03722, Republic of Korea. E-mail: dongil@yonsei.ac.kr*
[b] *Industrial Gas Research Cell, Research Institute of Industrial Science & Technology (RIST), Gwangyang-si 57801, Republic of Korea*

† Electronic supplementary information (ESI) available: Experimental methods, supplementary notes, photographic images, electrochemical data, thermal methanation data, TEM and corresponding EDS images, UV-Vis absorption spectra, cell configurations (Fig. S1–S11), and supplementary tables (Tables S1 and S2). See DOI: **https://doi.org/10.1039/d5ey00094g**

CO_2RR catalysts for CO production.[11–13] However, these catalysts typically exhibit polydispersity in size, shape, and surface structure, resulting in suboptimal activity and selectivity.[11]

Over the past decade, atomically precise metal nanoclusters (NCs) have emerged as a promising frontier in electrochemical CO_2RR.[14–16] Since Kauffman *et al.*'s pioneering report in 2012,[17] a variety of Au-, Ag-, and alloy-based NCs have been developed as CO_2RR electrocatalysts by tailoring their structures and compositions.[18–24] Notably, metal NCs have enabled atomic-level insights and driven significant advancements in electrocatalyst design. Using $Au_{25}(SR)_{18}$, $Au_{38}(SR)_{24}$, and $Au_{144}(SR)_{60}$ NCs (SR = thiolate) as model catalysts, we have demonstrated that these NCs undergo electrochemical activation *via* partial ligand loss, generating dethiolated Au sites that serve as active centers for CO_2-to-CO conversion.[25] Furthermore, the efficiency of CO_2-to-CO electroreduction can be enhanced by transplanting highly active Au sites into catalytically less-active $Ag_{25}(SR)_{18}$ and inactive $Ni_4(SR)_8$ NCs.[26,27] Additionally, the cation-relaying effect has been demonstrated to boost CO production on $Au_{25}(SR)_{18}$ NCs by employing anionic terminal groups on the protecting ligands.[28]

While significant progress has been made in developing selective CO_2RR catalysts for CO and formate production,[29] much less has been achieved toward developing catalysts for deep-reduced products such as CH_3OH, CH_4, and C_2H_4. Cu-based electrocatalysts have been widely employed for converting CO_2 into various deep-reduced products, owing to their appropriate adsorption energy for the *CO intermediate.[30–32] Ni-based electrocatalysts have also shown potential for hydrocarbon production.[33,34] However, low product purity remains a major challenge in the electrochemical CO_2RR process for deep-reduced products. For example, widely investigated deep-reduced products such as CH_3OH,[35,36] CH_4,[37–42] and C_2H_4,[43,44] typically exhibit purities below 30% due to the presence of undesired byproducts and unreacted CO_2. These impurities in the product stream necessitate additional separation steps, further emphasizing the challenge of achieving high-purity chemical production.

Thermocatalytic conversion of CO_2 is another promising strategy for producing deep-reduced products. This approach typically involves CO_2-to-CO conversion *via* the reverse water–gas shift (RWGS) reaction, followed by subsequent CO hydrogenation steps.[4–6] However, RWGS requires high temperatures due to its endothermic nature and also relies on external hydrogen sources,[45] significantly reducing the overall energy efficiency of the process. Cascade catalysis, which integrates electrochemical CO_2RR with thermochemical or biochemical reactions,[46–49] offers an effective alternative for producing deep-reduced products by bypassing the energy-intensive RWGS process. When combined with hydrocarbon production technologies such as CO methanation and Fischer–Tropsch synthesis, electrochemical CO_2RR could serve as a viable synthetic route for various deep-reduced chemicals and fuels.

Herein, we introduce an efficient cascade electro-thermocatalysis system for CH_4 production from CO_2. Electrochemical syngas was generated using CO_2RR-active electrocatalysts under varying CO_2 flow rates, including 1-hexanethiolate-protected Au_{25} [$Au_{25}(SC_6H_{13})_{18}$], 3,3-dimethyl-1-butynyl-protected Ag_{14} [$ClAg_{14}(C{\equiv}C{-}t\text{Bu})_{12}$], and Ag nanoparticles (Ag NPs). $Au_{25}(SC_6H_{13})_{18}$ and $ClAg_{14}(C{\equiv}C{-}t\text{Bu})_{12}$ are hereafter abbreviated as Au_{25} and Ag_{14}, respectively, throughout this paper. Among these, Ag_{14} NCs exhibited the highest carbon conversion efficiency, outperforming Au_{25} NCs and Ag NPs. Electrokinetic analysis indicated that the superior single-pass conversion efficiency (SPCE) of Ag_{14} NCs originates from their strong CO_2 binding affinity and exceptional CO selectivity. Ag_{14}-based electrolyzer was seamlessly integrated into a thermocatalysis reactor, achieving CH_4 production with a purity exceeding 85% at current densities ranging from 200–800 mA cm^{-2}. This integrated system effectively enhances product selectivity and SPCE, addressing key challenges in electrochemical CO_2-to-CH_4 conversion.

Results and discussion

Electrochemical production of CH_4 from CO_2 remains highly challenging owing to low selectivity and poor SPCE. On the other hand, thermal methanation of syngas is a well-established process capable of producing high-purity CH_4 when an appropriate syngas composition (H_2/CO = 3) is supplied.[50] In this study, we explore a cascade electro-thermocatalysis system consisting of a CO_2-to-syngas electrolyzer integrated with a thermal syngas methanation reactor. As illustrated in Scheme 1, CO_2 and water are first electrochemically converted into a mixture of CO and H_2 with a predetermined composition, which is then directly injected into the thermocatalysis reactor to produce high-purity CH_4. Notably, this system can be readily extended to produce several chemicals and fuels, such as lower olefins, gasoline, diesel, and more, by utilizing appropriate thermocatalysts and tailored syngas ratios.[4–6]

Electrochemical syngas production with tailored ratios has been achieved by employing a combination of CO_2RR and hydrogen evolution reaction (HER) catalysts that selectively produce CO and H_2 (eqn (1) and (2)).[51–54] However, this syngas production is typically conducted in excess CO_2, needing additional CO_2 separation from syngas product before it can be injected into the thermocatalysis reactor.[51] Furthermore, the

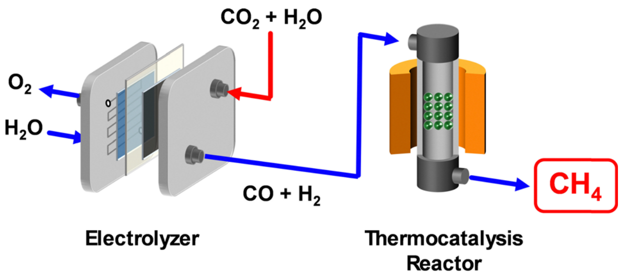

Scheme 1 Schematic of a cascade electro-thermocatalysis system for producing high-purity CH_4. The CO_2-electrolyzer generates CO_2-free syngas (CO + H_2), which is subsequently converted to CH_4 in the thermocatalysis reactor.

OH^- byproduct of HER may react with CO_2 to generate carbonates (eqn (3)), further reducing SPCE.

$$CO_2 + H_2O + 2e^- \rightarrow CO + 2OH^- \quad (1)$$

$$2H_2O + 2e^- \rightarrow H_2 + 2OH^- \quad (2)$$

$$CO_2 + 2OH^- \rightarrow CO_3^{2-} + H_2O \quad (3)$$

To minimize the fraction of unreacted CO_2 after CO_2RR, we explored the possibility of controlling the syngas ratio by adjusting the CO_2 flow rate. When CO_2RR is conducted using a highly efficient CO_2RR catalyst at a low CO_2 flow rate, CO_2-to-CO conversion would predominantly occur, with all supplied CO_2 being consumed before HER initiates. Thus, syngas ratio can be effectively controlled by adjusting CO_2 flow rate. Additionally, this approach is expected to significantly reduce carbonate production from HER byproduct.

It has been demonstrated that ligand-protected Au and Ag NCs exhibit high electrocatalytic activity for CO_2-to-CO conversion.[18–24,55] In this study, Au_{25} and Ag_{14} NCs were employed as CO_2RR catalysts owing to their exceptional CO selectivity and stability. The Au_{25} and Ag_{14} NCs were synthesized according to established protocols in the literature.[25,55] As shown in UV-Visible absorption spectra (Fig. S1, ESI†), synthesized NCs exhibit characteristic absorption peaks at 670 and 450 nm for Au_{25} NCs and 280 nm for Ag_{14} NCs. The homogeneity of the NCs, with average core diameters of 1.3 nm for Au_{25} and 1.2 nm for Ag_{14} NCs, was clearly observed in the transmission electron microscopy (TEM) images (Fig. S1, ESI†). These NCs were further characterized by electrospray ionization (ESI) mass spectrometry. As shown in Fig. 1a and b, intense single peaks for both NCs at *m/z* 7034 Da (orange line) and *m/z* 2520 Da (gray line) correspond to the $[Au_{25}(SC_6H_{13})_{18}]^-$ and $[ClAg_{14}(C_6H_9)_{12}]^+$ ions, respectively. The combined absorption and mass spectrometry analyses firmly establish the successful synthesis of the NCs, confirming their molecular purity.

CO_2RR activities of the synthesized Au_{25} and Ag_{14} NCs were evaluated in a zero-gap electrolyzer at a CO_2 flow rate of 50 mL min^{-1} (Fig. S2, ESI†). For comparison, commercial Ag NPs (Dioxide Materials) were also studied. NCs were immobilized in a gas diffusion electrode (GDE), which consisted of a microporous layer (MPL) and a gas diffusion layer (GDL). Fig. 1c presents CO_2RR activities of NC/GDE and Ag NP/GDE in the zero-gap cell at varying cell potentials (E_{cell}). Both NCs demonstrated higher CO_2RR activity than Ag NPs across the potential range. Additionally, current density for CO production (j_{CO}) on both NCs showed an exponential increase with increasing cell potential. Conversely, the Ag NPs exhibited a sharp decline in j_{CO} and CO selectivity at potentials above 2.5 V (Fig. 1d).

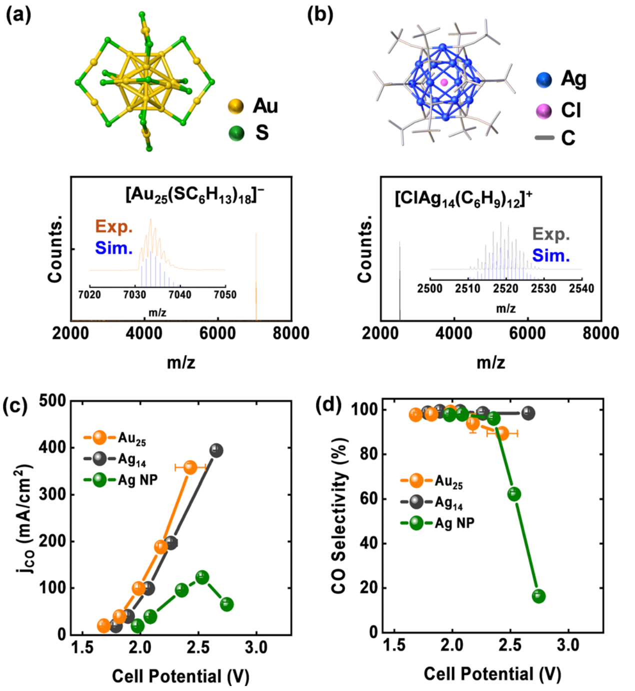

Fig. 1 Crystal structures (redrawn from ref. 56 and 57) and ESI mass spectra of (a) Au_{25} and (b) Ag_{14} NCs. All carbon atoms are omitted in panel (a) and displayed in wireframe form in panel (b) for clarity. Insets in panel (a) and (b) compare experimental data (lines) with the simulated isotope patterns (blue bars). The mass spectra of Au_{25} and Ag_{14} NCs were obtained in negative and positive ionization modes, respectively. (c) j_{CO} and (d) corresponding CO selectivities measured for Au_{25}/GDE-, Ag_{14}/GDE-, and Ag NP/GDE-equipped zero-gap CO_2 electrolyzers as functions of cell potential.

As illustrated in Fig. 1c, Au_{25} NCs exhibited the lowest cell potentials compared with other catalysts, with CO selectivity maintained above 97% within the potential range of 1.6–2.1 V. However, it dropped below 90% at higher cell potentials. Conversely, the Ag_{14} NCs achieved CO selectivity, exceeding 98% across the potential range. In a previous CO_2RR study, the exceptional CO selectivity of the Ag_{14} NCs was attributed to their unique adsorption properties, which facilitated enhanced CO_2-to-CO conversion and dramatically suppressed HER activity.[55]

There have been numerous attempts to achieve controlled syngas production with specific H_2/CO ratios by varying the applied potential or utilizing a combination of CO_2RR and HER catalysts.[51–54] In this study, we first investigated the controlled production of syngas using a combination of Au_{25} NCs and commercial Pt/C, which served as the CO_2RR-active and HER-active catalysts, respectively. Fig. 2a presents the results of electrolysis performed with the mixed catalysts at a current density of 200 mA cm^{-2}. As shown in the figure, CO fraction in the syngas can be precisely adjusted between 25 and 90% by varying the mixing ratio of the two catalysts. However, this approach led to over 60% of unreacted CO_2 in the product gas, which requires separation before injection into the thermo-catalysis reactor.

To address the issue of unreacted CO_2 remaining after syngas production, we explored the possibility of controlling CO fraction in syngas by adjusting the CO_2 flow rate. Highly efficient CO_2RR catalysts are essential to ensure that CO_2-to-CO conversion predominantly occurred, with all supplied CO_2 being consumed before HER initiates. Fig. S3 (ESI†) illustrates the CO and H_2 selectivities and the residual CO_2 fraction in the product gas at varying CO_2 flow rates. As shown in the figure,

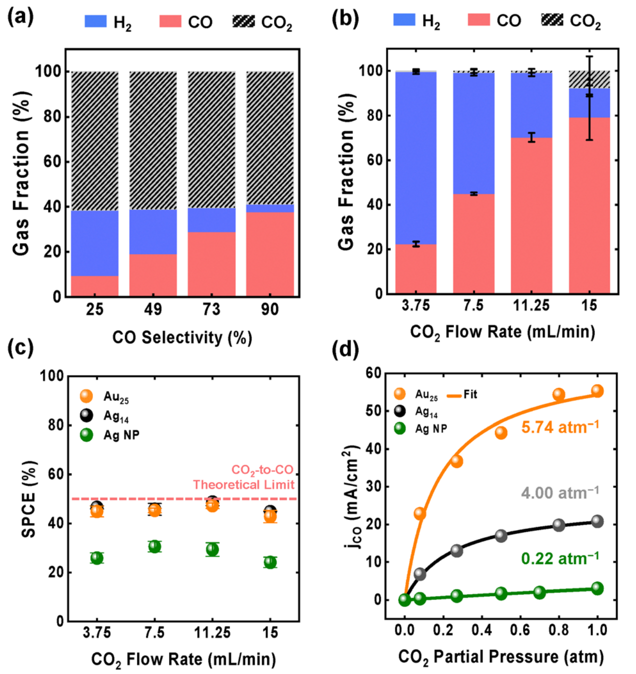

Fig. 2 Fractions of the product gas generated from mixed catalysts composed of Au_{25} NCs and Pt/C in the zero-gap electrolyzer at 200 mA cm^{-2} with a CO_2 flow rate of 30 mL min^{-1}. By employing different ratios of Au_{25} NCs to Pt/C in the mixed catalysts, various syngas compositions were achieved. (b) Fractions of the product gas generated from Au_{25} NCs at 200 mA cm^{-2} as a function of CO_2 flow rate, and (c) the corresponding SPCE. (d) j_{CO} of three electrocatalysts as a function of the CO_2 partial pressure at E_{cell} = 1.8 V (sphere). Total flow rate of the feed gas was 200 mL min^{-1}, and partial pressure of CO_2 was regulated using Ar gas. The binding affinity constants of the catalysts are described in the inset by fitting j_{CO}–P_{CO_2} plots with eqn (11) (solid line).

CO_2RR predominantly occurs over HER on the Au_{25} and Ag_{14} NCs, achieving CO selectivity greater than 90% at high flow rates (30–200 mL min^{-1}). At these flow rates, only a portion of the supplied CO_2 was converted into CO, leaving residual CO_2 to constitute over 60% of the product gas. CO selectivity gradually decreased, while H_2 production increased as the CO_2 flow rate was reduced below 15 mL min^{-1} (Fig. 2b). These results indicate that CO_2-to-CO conversion still occurs preferentially over HER even at low CO_2 flow rates, enabling control over syngas composition (*i.e.*, H_2/CO ratio) by varying the CO_2 flow rate. Notably, residual CO_2 fraction dramatically decreased to approximately zero at CO_2 flow rates below 15 mL min^{-1}.

Assuming the theoretical SPCE of 50% in alkaline CO_2-to-CO electroreduction,[58] the maximum j_{CO} and CO selectivity can be calculated based on the CO_2 flow rate (see the Supplementary Notes and Table S1 in the ESI†). For instance, CO selectivities of 25, 50, and 75% are expected at CO_2 flow rates of 3.75, 7.5, and 11.25 mL min^{-1}, respectively, at a total current density of 200 mA cm^{-2}. In Fig. S3 (ESI†), Au_{25} and Ag_{14} NCs achieve CO selectivities of 22 and 23%, respectively, which are close to the theoretical limit of 25% at a CO_2 flow rate of 3.75 mL min^{-1}. Actual SPCE values, calculated from these CO selectivities, were 45 and 46%, respectively, approaching the theoretical limit of 50% and significantly exceeding that of Ag NPs, which exhibited an SPCE of 27%. SPCE values obtained from the three catalysts at CO_2 flow rates ranging from 3.75–15 mL min^{-1} are presented in Fig. 2c. As depicted, Au_{25} and Ag_{14} NCs maintained SPCE values exceeding 43% across all flow rates. This result demonstrates that undesired CO_2 consumption due to HER can be effectively mitigated by employing highly efficient CO_2RR catalysts under controlled CO_2 supply conditions.

To understand the origin of the high SPCE observed for NCs during syngas production, an electrokinetic study was conducted in a kinetically controlled regime. A CO_2-fed flow electrolyzer was employed to monitor the cathode reaction (Fig. S4a, ESI†). As shown in Fig. S4 (ESI†), the Tafel slopes for Au_{25} and Ag_{14} NCs, obtained from a plot of log(j_{CO}) *versus* potential, were determined to be 40.7 and 42.0 mV dec^{-1}, respectively. Ag NPs exhibited a significantly higher Tafel slope of 131 mV dec^{-1}. This result strongly indicates that the mechanism of CO_2-to-CO electroreduction on the NCs is distinctly different from that of Ag NPs. CO_2-to-CO conversion under alkaline media can be described by the following elemental steps, where M* denotes the active site:

$$M^* + CO_2 + e^- \rightarrow M^*\text{–}CO_2^- \quad (4)$$

$$M^*\text{–}CO_2^- + H_2O \rightarrow M^*\text{–}COOH + OH^- \quad (5)$$

$$M^*\text{–}COOH + e^- \rightarrow M^*\text{–}COOH^- \quad (6)$$

$$M^*\text{–}COOH^- \rightarrow M^*\text{–}CO + OH^- \quad (7)$$

$$M^*\text{–}CO \rightarrow M^* + CO \quad (8)$$

Tafel slopes of 120 and 40 mV dec^{-1} indicate that the reaction is governed by the first [eqn (4)] and second [eqn (6)] electron transfer steps, respectively.[11,12,59,60] Since the proton transfer step could also play a role in the rate-determining step (RDS) of CO_2RR, a kinetic isotope effect (KIE) study using H/D was performed on the NC catalysts. Fig. S5 (ESI†) presents the j_{CO} values obtained from Au_{25} and Ag_{14} NCs as a function of applied potential in H_2O- and D_2O-based 1.0 M KOH solutions. Both NCs display approximately identical j_{CO} curves regardless of electrolyte condition, suggesting that the proton transfer step is not involved in the RDS for these NCs. Collectively, significantly low Tafel slopes observed for the NCs imply that the first electron transfer step is greatly facilitated on these NCs, while it constitutes the RDS for CO_2RR on Ag NPs.

To gain further mechanistic insights into CO_2RR on these NCs, we investigated the reaction order with respect to the CO_2 concentration. Fig. 2d shows the j_{CO} values measured at a cell potential of 1.8 V (*iR*-corrected) as a function of the partial pressure of CO_2 (P_{CO_2}) ranging from 0.1–1.0 atm. As shown in the figure, the j_{CO} *versus* P_{CO_2} plots for Au_{25} and Ag_{14} NCs exhibit concave curves, while the plot for Ag NPs is approximately linear. Concave curves observed for Au_{25} and Ag_{14} NCs are particularly notable, as they suggest exceptional CO_2RR activities even at low P_{CO_2}. This finding has practical implications for the direct conversion of diluted CO_2 without needing a concentration step.[61]

Concave curves can be analyzed using a modified Michaelis–Menten kinetic model.[25,61] In this model, the five elemental steps (eqn (4)–(8)) for CO_2-to-CO electroreduction are reduced to a two-step process. This process consists of a CO_2 binding step, forming an intermediate complex ($M^*{-}CO_2^-$), followed by a catalytic step that generates the CO product (eqn (9) and (10)):

$$M^* + CO_2 + e^- \underset{k_d}{\overset{k_a}{\rightleftharpoons}} M^*{-}CO_2^- \qquad (9)$$

$$M^*{-}CO_2^- \xrightarrow{k_{cat}} M^* + CO \qquad (10)$$

When the concentration of active sites is much lower than that of CO_2, a steady-state condition is rapidly established. In this state, the concentration of the $M^*{-}CO_2^-$ complex remains approximately constant over the timescale of product formation. The catalysis rate (j_{CO}) is then given by:

$$j_{CO} = \frac{nFk^{o}_{cat}K[M^*]_0P_{CO_2}}{1 + KP_{CO_2}}\exp\left(\frac{\beta\eta F}{RT}\right) \qquad (11)$$

where $K = \dfrac{k_a}{k_d + k_{cat}}$ represents the CO_2 binding affinity constant of the active site, k^{o}_{cat} is the standard rate constant, β is the symmetry factor, η is the overpotential, and other symbols are as commonly defined (see the Supplementary Notes for further details, ESI†).

Fitting the j_{CO}–P_{CO_2} plots in Fig. 2d with eqn (11) reveals that the P_{CO_2} dependence of j_{CO} is governed by K, the CO_2 binding affinity of the catalyst. Specifically, the j_{CO}–P_{CO_2} plot becomes concave when the catalyst exhibits a high CO_2 binding affinity (*i.e.*, $K \gg 1$). Conversely, the plot appears linear when the interaction between the catalyst and CO_2 is weak (*i.e.*, $K \ll 1$). The high K values of 5.74 and 4.00 atm^{-1}, determined for Au_{25} and Ag_{14}, respectively, explicitly indicate strong interactions between CO_2 and the catalyst, which underlie the exceptional CO_2RR activity and high SPCE. By contrast, the K value for Ag NPs is only 0.22 atm^{-1}, which accounts for the low SPCE observed in Fig. 2c.

In recent CO_2RR studies, Seong *et al.* demonstrated that Au_{25} and Ag_{14} NCs undergo electrochemical activation by losing some ligands, exposing de-ligated metal sites that serve as active sites.[25,55] Density functional theory (DFT) studies on Au_{25} and Ag_{14} NCs further revealed that the upshifted energy of the d-state in the Au and Ag active sites provides an optimal binding strength for CO_2 intermediates, leading to exceptional catalytic activity in the CO_2-to-CO conversion. CO_2 binding affinities determined for Au_{25} and Ag_{14} NCs demonstrate that they are sufficiently high to form stable intermediates, essential for the CO_2-to-CO conversion process. The high SPCE observed for Au_{25} and Ag_{14} NCs can be attributed to the unique CO_2-binding properties of the NCs, which enable high CO_2RR activity even under CO_2-deficient conditions.

To further assess syngas production under industrially relevant current densities, electrolysis was performed at current densities exceeding 200 mA cm^{-2}. Target CO selectivity was set at 25%, and the CO_2 flow rate was adjusted to achieve the predetermined j_{CO} at each current density. Fig. 3a and b illustrate the CO selectivity and corresponding SPCE values for three catalysts across a current density range of 200–800 mA cm^{-2}. As depicted in the figures, the CO selectivity of Au_{25} decreased significantly, from 22 to 15%, as the current density increased from 200 to 800 mA cm^{-2} (*i.e.*, with increasing overpotential). In contrast, the CO selectivity of Ag_{14} remained steady, ranging from 21 to 23%, irrespective of the current density. For Ag NPs, CO selectivity was 13% at 200 mA cm^{-2} and dropped below 7% at current densities over 400 mA cm^{-2}. Calculated SPCE values exhibited a similar trend. The SPCE of Au_{25} declined substantially, from 45 to 30%, as the current density increased, whereas the SPCE of Ag_{14} remained relatively constant, ranging from 42 to 47%, near the theoretical limit for CO_2-to-CO conversion in alkaline media. Meanwhile, the SPCE of Ag NPs decreased from 28% at 200 mA cm^{-2} to below 20% when the current density surpassed 400 mA cm^{-2}.

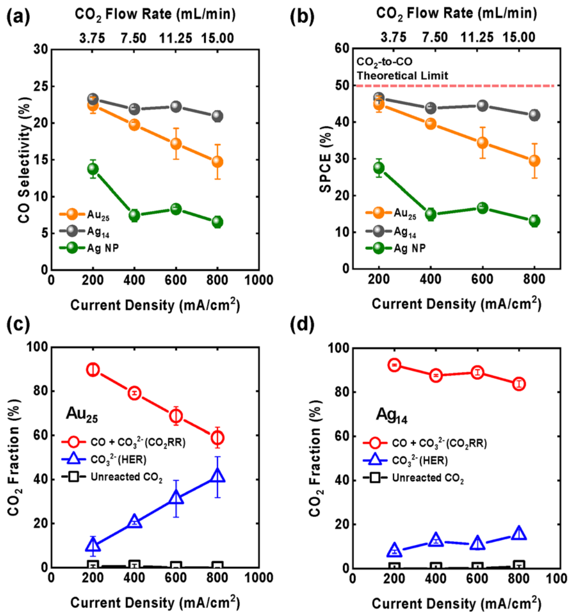

Fig. 3 (a) CO selectivities (b) SPCE obtained from Au_{25} and Ag_{14} NCs, and Ag NPs at a total current density range of 200–800 mA cm^{-2}. Fractions of CO_2 utilized during syngas production on (c) Au_{25} and (d) Ag_{14} NCs. CO + CO_3^{2-} (CO_2RR) represents the fraction of CO_2 consumed for CO production and CO_3^{2-} formation, whereas CO_3^{2-} (HER) denotes the CO_2 captured in CO_3^{2-} formation from the HER byproduct.

To understand the origin of the SPCE decrease, we analyzed the fraction of CO_2 utilized during electrolysis. Considering the theoretical limit of SPCE (50%) for CO_2-to-CO conversion in alkaline media, the SPCE of 45% observed for Au_{25} at 200 mA cm^{-2} indicates that most of the available CO_2 is consumed in the CO_2RR to produce CO. As the current density increased, SPCE decreased significantly, suggesting a decline in the fraction of CO_2 undergoing CO_2RR. Interestingly, unreacted CO_2 remained negligible across all current densities (Fig. 3c).

As shown in eqn (2), HER also generates OH^- ions, which can react with CO_2 to form carbonate ions. Therefore, CO_2 loss due to HER must be considered. Fig. 3c demonstrates that CO_2

capture into carbonate ions increased substantially for Au_{25} as HER activity intensified at higher current densities. Fractional analysis revealed that, for Ag NPs, there is not only carbonate formation from HER but also unreacted CO_2 (Fig. S6, ESI†). Conversely, carbonate formation due to HER remained low (Fig. 3d) for Ag_{14}, resulting in a consistently high SPCE of 42–47% across the current density range. This analysis underscores the importance of achieving superior CO selectivity over HER to maintain high SPCE for syngas production at elevated current densities.

The exceptional stability of Ag_{14} in sustaining CO selectivity and SPCE at elevated current densities establishes it as a promising candidate for industrial syngas production. To further evaluate its performance, we examined the long-term stability of syngas production at 400 mA cm^{-2} in a zero-gap electrolyzer with a flowing 1.0 M KOH electrolyte. CO_2 flow rate was adjusted to 8.7 mL min^{-1} to achieve a syngas ratio (H_2/CO) of 3. As shown in Fig. 4a, Ag_{14} NCs demonstrated excellent electrocatalytic stability, maintaining a cell potential of 2.7 V. CO selectivity was sustained at 25% over 24 h of operation, with the average SPCE value remaining consistent at 45 ± 2% (Fig. 4b). It is well-documented that alkaline CO_2RR in zero-gap electrolyzer faces challenges related to salt precipitation, which limits long-term operation at high current densities.[62] However, the syngas production approach proposed in this study utilizes an equivalent amount of CO_2 to achieve the desired ratio, effectively preventing salt precipitation over 24 h of operation (Fig. S7a, ESI†). Conversely, supplying 200 mL min^{-1} of CO_2 at the same current density led to massive salt precipitation within 1 h (Fig. S7b, ESI†). These results demonstrate that highly pure syngas with the desired H_2/CO ratio can be efficiently produced by employing highly CO-selective Ag_{14} NCs and controlling the CO_2 supply.

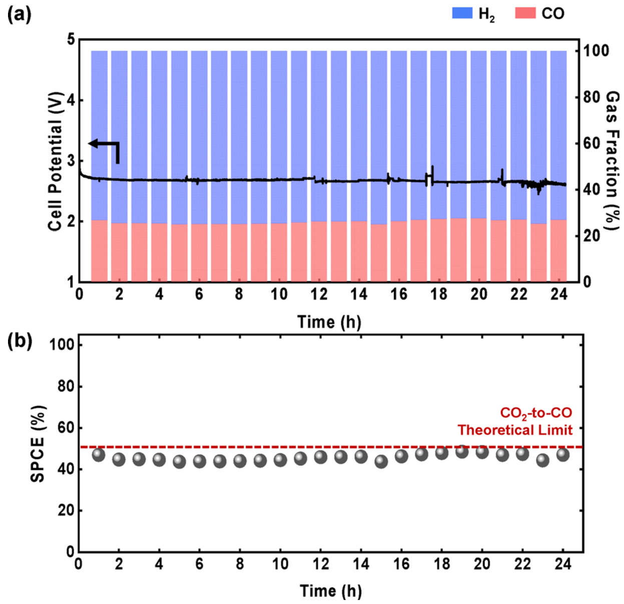

Fig. 4 (a) Gas fractions and cell potentials, and (b) corresponding SPCE values recorded during electrochemical syngas production on Ag_{14} NCs for 24 h at 400 mA cm^{-2}. A 1.0 M KOH (3.0 mL min^{-1}) and CO_2 gas (8.7 mL min^{-1}) were supplied to the anode and cathode sides of the zero-gap electrolyzer, respectively.

High SPCE syngas production on Ag_{14} motivated us to explore CH_4 production by directly integrating the zero-gap electrolyzer into a thermocatalysis process, as illustrated in Fig. 5a. Ni-based catalysts are widely used for CH_4 production owing to their high conversion efficiency and selectivity at low temperatures of 250–400 °C.[50,63] Therefore, we employed a Ni-based Si/Al/Mg zeolite (referred to as Ni-zeolite hereafter) as the thermocatalyst. The catalyst was synthesized *via* the co-precipitation method following established literature protocols (see ESI† for details).[64] Fig. S8a (ESI†) presents high-resolution TEM results and energy dispersive X-ray spectroscopy (EDS) map images of the Ni-zeolite catalyst. As shown in the figure, Ni nanoparticles are uniformly deposited on the Si/Al/Mg-based zeolite support. Quantitative analysis revealed that the Ni-zeolite catalyst comprises 52 wt% Ni/NiO, 34 wt% Al_2O_3, 6 wt% SiO_2, and 7 wt% MgO. X-ray diffraction (XRD) patterns of the catalyst in Fig. S8b (ESI†) exhibit characteristic peaks for metallic Ni and NiO, confirming that the synthesized Ni nanoparticles possess a mixed valence state. Additionally, polymorphic SiO_2 chabazite was prominently observed in the XRD patterns.[65]

As a syngas ratio of H_2/CO = 3 is required to produce highly pure CH_4, the CO_2 flow rates were adjusted to achieve 25% CO selectivity at the applied current densities. Fig. S9 (ESI†) shows the product gas selectivities at various current densities obtained from the Ag_{14}/GDE-equipped electrolyzer. As shown in the figure, the product gas consistently contained 25.5 and 74.5% CO and H_2, respectively, across all current densities, indicating that the desired syngas ratio was successfully achieved by regulating CO_2 flow rates. Notably, the residual CO_2 in the product gas was less than 1% at all current densities. The produced syngas was then directly injected into the thermocatalysis reactor, where the reactor bed temperature was set to 300 °C. This temperature demonstrated the highest conversion efficiency among the temperatures investigated (Fig. S10, ESI†).

Fig. 5b presents the product gas selectivities of the cascade electro-thermocatalysis system across a current range of 200–800 mA cm^{-2}. Results clearly show that the electrochemically produced syngas was directly converted into high-purity CH_4, achieving a CH_4 concentration exceeding 85%. Notably, almost all CO in the syngas was successfully converted to CH_4. The presence of approximately 1% residual CO_2 is attributed to the thermodynamic equilibrium of the syngas-to-CH_4 conversion at 1 atm.[50] However, the product gas contained slightly more H_2 than theoretically expected (<5%). Based on the product concentration, the initial CO selectivity was calculated to be 24.5%, which is 1% lower than the syngas production results shown in Fig. S9 (ESI†). This discrepancy is attributed to the back pressure from the methanation reactor, which caused additional CO_2 loss and a subsequent reduction in CO selectivity in the electrolyzer due to CO_2 dissolution into the electrolyte. We believe that managing the pressure balance between the

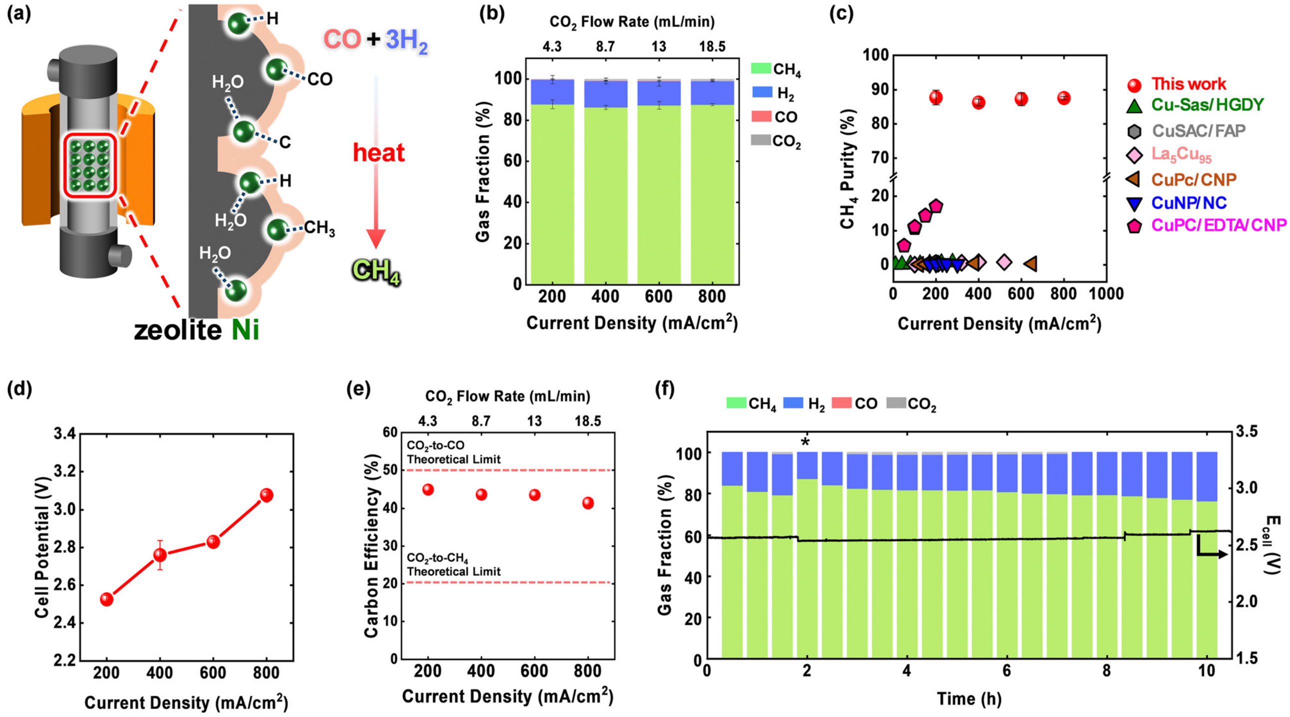

Fig. 5 (a) A schematic of the syngas-to-CH_4 conversion in a thermal reactor with an inner diameter of 11.2 mm and a length of 35 cm, packed with Ni-zeolite catalyst particles. The desired syngas ratio (H_2/CO = 3) was achieved by adjusting CO_2 flow rates at each current density, and the thermocatalysis reactor temperature was maintained at 300 °C throughout the experiment. (b) Fractions of the product gas obtained from the cascade electro-thermocatalysis system. (c) Comparison of CH_4 purity in the product gas from the cascade system with data from direct electrochemical CO_2-to-CH_4 conversion reported in prior studies.[37–42] (d) Cell potentials of the electrolyzer and (e) carbon conversion efficiency obtained from the terminal gas stream of the cascade system. (f) Long-term stability of methane production using the cascade system. Product gas selectivity and cell potential were recorded for 10 h at 400 mA cm^{-2}. The asterisk mark at the 2 h mark indicates when the connection between the electrolyzer and thermal reactor was temporarily disconnected and reconnected to assess back-pressure issues.

electrolyzer and the thermal reactor in large-scale experiments could mitigate this issue, thereby improving CH_4 purity further.

Despite advancements in selective CO_2-to-CH_4 conversion electrocatalysts, achieving high product gas purity remains challenging owing to the excess amount of unreacted CO_2.[37–42] Fig. 5c and Table S2 (ESI†) compare the CH_4 purity of the product gas achieved using the cascade electro-thermocatalysis system with that of other electrochemical systems. As shown in the figure, the CH_4 purity and current density achieved by the cascade system are significantly higher than those obtained through direct CO_2-to-CH_4 electrocatalysis.[37–42] These results strongly suggest that coupling electrochemical syngas production with a thermal methanation process is a highly feasible approach for producing high-purity CH_4.

Furthermore, the Ag_{14}-based cascade electro-thermocatalysis system demonstrated outstanding syngas production performance across all current densities. At total current densities of 200 and 800 mA cm^{-2}, the cell potential reached 2.5 and 3.1 V, respectively, which are significantly lower than those reported for other catalysts used in CH_4 production (Fig. S11, ESI†). Given that CO_2-to-CH_4 electroreduction typically requires high overpotentials,[37–42,66,67] the production of CO at significantly lower overpotentials offers a distinct advantage of the cascade system (Table S2, ESI†). Additionally, since methanation is an exothermic reaction, the energy input required for the thermocatalysis process during operation would be minimal, and the waste heat generated could be effectively utilized for supplementary processes, such as power generation.[68]

Based on the CO and CH_4 selectivities obtained from the electrolyzer and thermal reactor, carbon conversion efficiency of the entire cascade system was calculated. Combined with the near-theoretical SPCE from electrolysis and the exceptional CO conversion efficiency during methanation, overall carbon conversion efficiency reached 45% at 200 mA cm^{-2} and slightly decreased to 41% at 800 mA cm^{-2} (Fig. 5e) owing to enhanced HER at higher current densities. Notably, the cascade system surpasses the theoretical limit of CO_2-to-CH_4 electroreduction in alkaline media (20%), where the remaining 80% of CO_2 is typically captured as carbonate ions. Notably, the cascade electro-thermocatalysis system can be readily adapted for multi-carbon product generation, which often faces challenges of low carbon conversion efficiency owing to poor product selectivity and extensive carbonate formation.

Finally, long-term stability of the cascade system was evaluated by monitoring E_{cell} and product selectivity at a current density of 400 mA cm^{-2}. As presented in Fig. 5f, the cascade system exhibited reasonable stability, maintaining an E_{cell} of 2.7 V during 10 h of operation. The gradual decline in CH_4

selectivity is thought to be due to the back pressure of the methanation reactor, which caused a reduction in CO selectivity. In fact, the CH_4 selectivity was recovered to 87% after disconnecting and reconnecting the electrolyzer and thermal reactor at a reaction time of 2 h, confirming the back-pressure issue in the system. Nevertheless, CH_4 purity was maintained above 78%, with negligible residual CO_2 during the 10-h operation. This surpasses the CH_4 purity achieved through direct CO_2-to-CH_4 electrocatalysis. These results demonstrate that the cascade electro-thermocatalysis system offers highly selective and stable CH_4 production with superior carbon conversion efficiency.

Conclusions

The efficient cascade electro-thermocatalysis system for high-purity CH_4 production from CO_2 was successfully demonstrated. Electrochemical syngas production was conducted using CO_2RR-active electrocatalysts, specifically Au_{25} and Ag_{14} NCs, and Ag NPs, by regulating CO_2 flow rates. Au_{25} and Ag_{14} NCs exhibited near-theoretical SPCE during syngas production at low CO_2 flow rates, whereas Ag NPs displayed low SPCE with unreacted CO_2 present in the product gas. Electrokinetic analyses performed on these catalysts revealed that the high CO_2RR activities of Au_{25} and Ag_{14} NCs under CO_2-deficient conditions originated from their high CO_2 binding affinities, which facilitate the otherwise sluggish first electron transfer step. Syngas production at higher current densities exceeding 200 mA cm^{-2} revealed that, unlike Au_{25}, CO selectivity for Ag_{14} remained high across the current density range of 200–800 mA cm^{-2}, demonstrating that exceptional CO selectivity is required to achieve high SPCE at elevated current densities. The Ag_{14}-equipped electrolyzer, integrated with a Ni-based thermocatalysis reactor, achieved CH_4 production with a purity exceeding 85% across all current densities. These results highlight the potential of integrating electrochemical and thermocatalytic processes for high-purity methane production and open avenues for value-added hydrocarbon production.

Author contributions

S. M. H., J. K., and D. L. designed the project. S. M. H., M. P., and S. K. conducted catalyst synthesis and electrochemical experiments. S. M. H., S. K., and C. J. conducted thermocatalysis experiments. J. K. and D. L. supervised the project. S. M. H. and D. L. wrote and revised the manuscript. All authors discussed the results and provided comments on the manuscript at all stages.

Data availability

The data supporting this article have been included as part of the ESI.†

Conflicts of interest

There are no conflicts to declare.

Acknowledgements

This work was supported by the National Research Foundation of Korea (NRF) grants (no. NRF-2022R1A2C3003610, RS-2024-00359914) and the Carbon-to-X Project (Project no. 2020M3H7A1096388) through the NRF funded by the Ministry of Science and ICT, Republic of Korea. This work was supported in part by the Yonsei University Research Fund (Post Doc. Researcher Supporting Program) of 2024 (project no.: 2024-12-0026).

Notes and references

1 C. Costentin, M. Robert and J. M. Saveant, *Chem. Soc. Rev.*, 2013, **42**, 2423–2436.
2 J. Qiao, Y. Liu, F. Hong and J. Zhang, *Chem. Soc. Rev.*, 2014, **43**, 631–675.
3 P. De Luna, C. Hahn, D. Higgins, S. A. Jaffer, T. F. Jaramillo and E. H. Sargent, *Science*, 2019, **364**, eaav3506.
4 Y. Chen, J. Wei, M. S. Duyar, V. V. Ordomsky, A. Y. Khodakov and J. Liu, *Chem. Soc. Rev.*, 2021, **50**, 2337–2366.
5 G. Bozzano and F. Manenti, *Prog. Energy Combust. Sci.*, 2016, **56**, 71–105.
6 G. Liu, G. Yang, X. Peng, J. Wu and N. Tsubaki, *Chem. Soc. Rev.*, 2022, **51**, 5606–5659.
7 C. Higman and S. Tam, *Chem. Rev.*, 2014, **114**, 1673–1708.
8 A. Ugwu, A. Zaabout, F. Donat, G. van Diest, K. Albertsen, C. Müller and S. Amini, *Ind. Eng. Chem. Res.*, 2021, **60**, 3516–3531.
9 S. Lu, Y. Shi, N. Meng, S. Lu, Y. Yu and B. Zhang, *Cell Rep. Phys. Sci.*, 2020, **1**, 100237.
10 Y. Hua, J. Wang, T. Min and Z. Gao, *J. Power Sources*, 2022, **535**, 231453.
11 Y. Chen, C. W. Li and M. W. Kanan, *J. Am. Chem. Soc.*, 2012, **134**, 19969–19972.
12 S. Verma, Y. Hamasaki, C. Kim, W. X. Huang, S. Lu, H. R. M. Jhong, A. A. Gewirth, T. Fujigaya, N. Nakashima and P. J. A. Kenis, *ACS Energy Lett.*, 2018, **3**, 193–198.
13 W. Zhu, R. Michalsky, O. Metin, H. Lv, S. Guo, C. J. Wright, X. Sun, A. A. Peterson and S. Sun, *J. Am. Chem. Soc.*, 2013, **135**, 16833–16836.
14 K. Kwak and D. Lee, *Acc. Chem. Res.*, 2019, **52**, 12–22.
15 B. Kumar, T. Kawawaki, N. Shimizu, Y. Imai, D. Suzuki, S. Hossain, L. V. Nair and Y. Negishi, *Nanoscale*, 2020, **12**, 9969–9979.
16 S. Zhao, R. Jin and R. Jin, *ACS Energy Lett.*, 2018, **3**, 452–462.
17 D. R. Kauffman, D. Alfonso, C. Matranga, H. Qian and R. Jin, *J. Am. Chem. Soc.*, 2012, **134**, 10237–10243.
18 Z. H. Gao, K. C. Wei, T. Wu, J. Dong, D. E. Jiang, S. H. Sun and L. S. Wang, *J. Am. Chem. Soc.*, 2022, **144**, 5258–5262.

19 S. T. Li, A. V. Nagarajan, D. R. Alfonso, M. K. Sun, D. R. Kauffman, G. Mpourmpakis and R. C. Jin, *Angew. Chem., Int. Ed.*, 2021, **60**, 6351–6356.

20 J. Wang, F. Xu, Z. Y. Wang, S. Q. Zang and T. C. W. Mak, *Angew. Chem., Int. Ed.*, 2022, **61**, e202207492.

21 S. Yoo, S. Yoo, G. Deng, F. Sun, K. Lee, H. Jang, C. W. Lee, X. L. Liu, J. Jang, Q. Tang, Y. J. Hwang, T. Hyeon and M. S. Bootharaju, *Adv. Mater.*, 2024, **36**, 2313032.

22 Z. Liu, J. Chen, B. Li, D. E. Jiang, L. Wang, Q. Yao and J. Xie, *J. Am. Chem. Soc.*, 2024, **146**, 11773–11781.

23 L. Luo, X. Zhou, Y. Chen, F. Sun, L. Wang and Q. Tang, *Chem. Sci.*, 2025, **16**, 3598–3610.

24 L. Qin, F. Sun, X. Ma, G. Ma, Y. Tang, L. Wang, Q. Tang, R. Jin and Z. Tang, *Angew. Chem., Int. Ed.*, 2021, **60**, 26136–26141.

25 H. Seong, V. Efremov, G. Park, H. Kim, J. S. Yoo and D. Lee, *Angew. Chem., Int. Ed.*, 2021, **60**, 14563–14570.

26 H. Seong, Y. Jo, V. Efremov, Y. Kim, S. Park, S. M. Han, K. Y. Chang, J. Park, W. Choi, W. Kim, C. H. Choi, J. S. Yoo and D. Lee, *J. Am. Chem. Soc.*, 2023, **145**, 2152–2160.

27 H. Seong, M. Choi, S. Park, H. W. Kim, J. Kim, W. Kim, J. S. Yoo and D. Lee, *ACS Energy Lett.*, 2022, **7**, 4177–4184.

28 S. M. Han, M. Park, J. Kim and D. Lee, *Angew. Chem., Int. Ed.*, 2024, **63**, e202404387.

29 Y. Lei, Z. Wang, A. Bao, X. Tang, X. Huang, H. Yi, S. Zhao, T. Sun, J. Wang and F. Gao, *Chem. Eng. J.*, 2023, **453**, 139663.

30 S. Nitopi, E. Bertheussen, S. B. Scott, X. Liu, A. K. Engstfeld, S. Horch, B. Seger, I. E. L. Stephens, K. Chan, C. Hahn, J. K. Norskov, T. F. Jaramillo and I. Chorkendorff, *Chem. Rev.*, 2019, **119**, 7610–7672.

31 Q. J. Wu, D. H. Si, P. P. Sun, Y. L. Dong, S. Zheng, Q. Chen, S. H. Ye, D. Sun, R. Cao and Y. B. Huang, *Angew. Chem., Int. Ed.*, 2023, **62**, e202306822.

32 J. K. Li, J. P. Dong, S. S. Liu, Y. Hua, X. L. Zhao, Z. J. Li, S. N. Zhao, S. Q. Zang and R. Wang, *Angew. Chem., Int. Ed.*, 2024, **63**, e202412144.

33 Y. Zhou, A. J. Martín, F. Dattila, S. Xi, N. López, J. Pérez-Ramírez and B. S. Yeo, *Nat. Catal.*, 2022, **5**, 545–554.

34 T. Wang, X. Duan, R. Bai, H. Li, C. Qin, J. Zhang, Z. Duan, K. J. Chen and F. Pan, *Adv. Mater.*, 2024, **36**, 2410125.

35 X. Yang, J. Cheng, X. Yang, Y. Xu, W. F. Sun and J. H. Zhou, *Chem. Eng. J.*, 2022, **431**, 134171.

36 H. Yu, X. Han, Z. Hua, W. Yang, X. Wu, Y. Wu, S. Chen, W. Hong, S. Deng, J. Zhang and J. Wang, *ACS Catal.*, 2024, **14**, 12783–12791.

37 P. Zhao, H. Jiang, H. Shen, S. Yang, R. Gao, Y. Guo, Q. Zhang and H. Zhang, *Angew. Chem., Int. Ed.*, 2023, **62**, e202314121.

38 Y. Wu, C. Chen, X. Yan, R. Wu, S. Liu, J. Ma, J. Zhang, Z. Liu, X. Xing, Z. Wu and B. Han, *Chem. Sci.*, 2022, **13**, 8388–8394.

39 Y. Xu, F. Li, A. Xu, J. P. Edwards, S. F. Hung, C. M. Gabardo, C. P. O'Brien, S. Liu, X. Wang, Y. Li, J. Wicks, R. K. Miao, Y. Liu, J. Li, J. E. Huang, J. Abed, Y. Wang, E. H. Sargent and D. Sinton, *Nat. Commun.*, 2021, **12**, 2932.

40 J. Li, Y. Jiang, J. Li, X. Wang, H. Liu, N. Zhang, R. Long and Y. Xiong, *Nanoscale*, 2023, **16**, 171–179.

41 M. Fan, R. K. Miao, P. Ou, Y. Xu, Z. Y. Lin, T. J. Lee, S. F. Hung, K. Xie, J. E. Huang, W. Ni, J. Li, Y. Zhao, A. Ozden, C. P. O'Brien, Y. Chen, Y. C. Xiao, S. Liu, J. Wicks, X. Wang, J. Abed, E. Shirzadi, E. H. Sargent and D. Sinton, *Nat. Commun.*, 2023, **14**, 3314.

42 J. Zhao, P. Zhang, T. Yuan, D. Cheng, S. Zhen, H. Gao, T. Wang, Z. J. Zhao and J. Gong, *J. Am. Chem. Soc.*, 2023, **145**, 6622–6627.

43 S. Chen, C. Ye, Z. Wang, P. Li, W. Jiang, Z. Zhuang, J. Zhu, X. Zheng, S. Zaman, H. Ou, L. Lv, L. Tan, Y. Su, J. Ouyang and D. Wang, *Angew. Chem., Int. Ed.*, 2023, **62**, e202315621.

44 S. Chen, X. Zheng, P. Zhu, Y. Li, Z. Zhuang, H. Wu, J. Zhu, C. Xiao, M. Chen, P. Wang, D. Wang and Y. L. He, *Angew. Chem., Int. Ed.*, 2024, **63**, e202411591.

45 P. Kaiser, R. B. Unde, C. Kern and A. Jess, *Chem. Ing. Tech.*, 2013, **85**, 489–499.

46 M. G. Lee, X. Y. Li, A. Ozden, J. Wicks, P. Ou, Y. Li, R. Dorakhan, J. Lee, H. K. Park, J. W. Yang, B. Chen, J. Abed, R. dos Reis, G. Lee, J. E. Huang, T. Peng, Y. H. Chin, D. Sinton and E. H. Sargent, *Nat. Catal.*, 2023, **6**, 310–318.

47 M. Cui, Q. Qian, J. Zhang, Y. Wang, B. B. A. Bediako, H. Liu and B. Han, *Chem*, 2021, **7**, 726–737.

48 W. Zheng, X. Yang, Z. Li, B. Yang, Q. Zhang, L. Lei and Y. Hou, *Angew. Chem., Int. Ed.*, 2023, **62**, e202307283.

49 J. Zhang, X. Kang, Y. Yan, X. Ding, L. He and Y. Li, *Angew. Chem., Int. Ed.*, 2024, **63**, e202315777.

50 J. Gao, Y. Wang, Y. Ping, D. Hu, G. Xu, F. Gu and F. Su, *RSC Adv.*, 2012, **2**, 2358–2368.

51 Y. Chen, M. Xia, C. Zhou, Y. Zhang, C. Zhou, F. Xu, B. Feng, X. Wang, L. Yang, Z. Hu and Q. Wu, *ACS Nano*, 2023, **17**, 22095–22105.

52 J. Wang, Q. Xiang, W. Zhang, F. Shi, F. Li, P. Tao, C. Song, W. Shang, T. Deng and J. Wu, *ACS Appl. Energy Mater.*, 2022, **5**, 5531–5539.

53 M. Zhang, Z. Hu, L. Gu, Q. Zhang, L. Zhang, Q. Song, W. Zhou and S. Hu, *Nano Res.*, 2020, **13**, 3206–3211.

54 I. Sanjuán, V. Kumbhar, V. Chanda, R. R. L. Machado, B. N. Jaato, M. Braun, M. A. A. Mahbub, G. Bendt, U. Hagemann, M. Heidelmann, W. Schuhmann and C. Andronescu, *Small*, 2024, **20**, 2305958.

55 H. Seong, K. Chang, F. Sun, S. Lee, S. M. Han, Y. Kim, C. H. Choi, Q. Tang and D. Lee, *Adv. Sci.*, 2023, **11**, 2306089.

56 M. Zhu, C. M. Aikens, F. J. Hollander, G. C. Schatz and R. Jin, *J. Am. Chem. Soc.*, 2008, **130**, 5883–5885.

57 D. Rais, J. Yau, D. M. P. Mingos, R. Vilar, A. J. P. White and D. J. Williams, *Angew. Chem., Int. Ed.*, 2001, **40**, 3464–3467.

58 J. A. Rabinowitz and M. W. Kanan, *Nat. Commun.*, 2020, **11**, 5231.

59 T. Shinagawa, A. T. Garcia-Esparza and K. Takanabe, *Sci. Rep.*, 2015, **5**, 13801.

60 M. Dunwell, W. Luc, Y. Yan, F. Jiao and B. Xu, *ACS Catal.*, 2018, **8**, 8121–8129.

61 B. Kim, H. Seong, J. T. Song, K. Kwak, H. Song, Y. C. Tan, G. Park, D. Lee and J. Oh, *ACS Energy Lett.*, 2020, **5**, 749–757.

62 Y. Xu, J. P. Edwards, S. Liu, R. K. Miao, J. E. Huang, C. M. Gabardo, C. P. O'Brien, J. Li, E. H. Sargent and D. Sinton, *ACS Energy Lett.*, 2021, **6**, 809–815.

63 M. Gruber, P. Weinbrecht, L. Biffar, S. Harth, D. Trimis, J. Brabandt, O. Posdziech and R. Blumentritt, *Fuel Process. Technol.*, 2018, **181**, 61–74.

64 C. E. Yeo, M. Seo, D. Kim, C. Jeong, H. S. Shin and S. Kim, *Energies*, 2021, **14**, 8414.

65 M. J. Díaz-Cabañas, P. A. Barrett and M. A. Camblor, *Chem. Commun.*, 1998, 1881–1882, DOI: **10.1039/a804800b**.

66 Y. Li, A. Xu, Y. Lum, X. Wang, S. F. Hung, B. Chen, Z. Wang, Y. Xu, F. Li, J. Abed, J. E. Huang, A. S. Rasouli, J. Wicks, L. K. Sagar, T. Peng, A. H. Ip, D. Sinton, H. Jiang, C. Z. Li and E. H. Sargent, *Nat. Commun.*, 2020, **11**, 6190.

67 M. Salehi, H. Al-Mahayni, A. Farzi, M. McKee, S. Kaviani, E. Pajootan, R. Lin, N. Kornienko and A. Seifitokaldani, *Appl. Catal., B*, 2024, **353**, 124061.

68 S. Morimoto, N. Kitagawa, N. Thuy, A. Ozawa, R. A. Rustandi and S. Kataoka, *J. CO2 Util.*, 2022, **58**, 101935.